In vivo NMR of hyperpolarized ^{3}He in the human lung at very low magnetic fields

Christopher P. Bidinosti,* Jamal Choukeife, Pierre-Jean Nacher,
and Geneviève Tastevin

Laboratoire Kastler Brossel, 24 rue Lhomond, F75231 Paris, France[1]

Abstract

We present NMR measurements of the diffusion of hyperpolarized ^{3}He in the human lung performed at fields much lower than those of conventional MRI scanners. The measurements were made on standing subjects using homebuilt apparatus operating at 3 mT. O_2-limited transverse relaxation (T_2 up to 15–35 s) could be measured in vivo. Accurate global diffusion measurements have been performed in vivo and in a plastic bag; the average apparent diffusion coefficient (ADC) in vivo was $14.2 \pm 0.6\,\mathrm{mm^2/s}$, whereas the diffusion coefficient in the bag (^{3}He diluted in N_2) was $79.5 \pm 1\,\mathrm{mm^2/s}$. 1D ADC mapping with high SNR ($\sim$200–300) demonstrates the real possibility of performing quality lung imaging at extremely low fields.
© 2003 Elsevier Science (USA). All rights reserved.

Keywords: Hyperpolarised helium; Lung imaging; Diffusion; ADC

1. Introduction

The first demonstrations of very low field MRI using a hyperpolarized noble gas were done about four years ago, first in glass and plastic cells [1], and subsequently in excised rat lungs [2]. These measurements were performed at $\sim$2 mT with a homebuilt instrument, and showed, in convincing fashion, the feasibility of generating MR images with hyperpolarized gas (HG) in magnetic fields that are otherwise far too weak to have produced a useful thermal Boltzmann polarization. There are many possible uses for this technique including medical imaging. In this paper we present a realization of this idea through the first measurements of the apparent diffusion coefficient (ADC) of hyperpolarized ^{3}He in the human lung at very low field (3 mT).

The very first use of HG to image a biological system was reported in 1994; here, the excised heart and lungs of a mouse where imaged using hyperpolarized ^{129}Xe in a commercial NMR unit operating at 9.4 T field [3]. In vivo studies on the human lung began in 1996 using conventional clinical systems operating at 0.8 T [4,5] and 1.5 T [6]. However, unlike conventional MRI, the strong field is not needed here to polarize the gas. Futhermore, if experimental noise is dominated by electrical losses in the body it scales linearly with frequency [7], and because the inductive NMR signal does so as well, the signal-to-noise ratio (SNR) is independent of field and there exists no benefit to performing HG imaging at high fields in that respect. This was confirmed at 0.1 T by the research group at Orsay using a Sopha-imaging-Magnetech MRI unit [8,9].

Still, all in vivo HG studies reported to date have employed *high field* magnets designed for proton imaging, a fact most likely due to the reason that researchers have found it convenient for the moment to simply adopt existing technology. The question remains, however, at which field strength could HG imaging prove itself most useful for medical diagnostics and will this warrant the development of specialized HG scanners?

From this point of view, there are several compelling arguments to investigate very low field (<0.1 T) HG imaging. We list them here as the underlying motivation for the work presented in this paper.

(a) *Field-independent SNR.* As mentioned, there is no reduction in SNR at lower fields if RF losses in the body dominate the noise. However, below some frequency the body becomes transparent to the RF and the Johnson noise of the detection coils will subsequently dominate. Coil-dominated noise depends on the field as $B^{1/4}$ [7], so one expects the SNR to vary as $B^{3/4}$ at very low fields. The frequency at which this cross-over occurs has yet to be established experimentally, but it is expected to be larger than the 102 kHz used in our study here. From this point of view, a larger field strength may be preferable; however, one should note that a lower than optimal SNR will not necessarily preclude operation in the very low field regime, as there may exist a desirable trade-off with the other possible benefits.

(b) *Reduced susceptibility gradients.* Spatial variations in tissue susceptibility produce local field gradients whose magnitude is proportional to the applied field. This can be problematic for lung imaging at high fields, where differences of magnetic susceptibility between blood vessels, lung tissue and airspaces produce very strong gradients.

(c) *Reduced power absorption rate.* RF power absorption rates decrease with frequency. Therefore, operation at lower fields will allow the use of new, rapid pulse sequences without exceeding the safety limit of 4 W/kg of absorbed power. This has been demonstrated at 0.1 T [9] with π-pulse repetition times as short as 10 ms.

(d) *Novel detection methods.* It may be possible to develop innovative signal detectors that offer improved performance at low field, but would otherwise be impractical for use at high field. Possible examples include networks of local detectors, superconducting coils, and SQUID detectors and amplifiers.

(e) *Novel scanner geometries.* Very low field scanners will not require cryogenics (to cool superconducting magnets) nor be encumbered by massive resistive or permanent magnets. This will permit unparalleled flexibility in scanner design. For example, a less bulky system may allow for measurements to be made with the subject either standing or supine, which might be of interest in pulmonary research.

(f) *Low cost, dedicated scanners for pulmonary research.* There is strong evidence that the occurrence of certain lung pathologies, such as asthma and chronic obstructive pulmonary disease (COPD), is increasing, and that HG imaging could provide improved diagnosis and assessment of these prevalent afflictions [10]. Should the usefulness of this technique become convincingly established, demands for time on existing conventional scanners could increase dramatically. Very low field,

HG scanners should be relatively inexpensive to purchase and operate, and as a result, they might one day find a use in this research area.

Having put forth these proposed benefits, we also point out certain challenges that may exist in performing very low field HG imaging. First, as stated above, SNR will eventually degrade with reduced field. As a result, operating at too low a field would most likely force one to reduce Johnson noise by means of a cryogenic system to cool conventional or superconducting pick-up coils. Another challenge may also arise if one attempts to make ultrafast diffusion measurements or imaging. In this case, the strong applied gradients may have longitudinal and transverse components that approach, or even exceed, the amplitude of the uniform applied magnetic field, thereby precluding straightforward operation [11–13]. For example, an applied gradient of 15 mT/m would result in additional field components up to $\sim\pm2$ mT over the region of the lung; to determine ADC values using such a gradient at very low B_0 field (such as 3 mT), one would have to abandon the usual high field approximation and consider a more exact calculation involving diffusion along the line gradient of the total magnetic field [11].

To move well beyond the point of conjecture and to truly examine the potential of very low field lung imaging with hyperpolarized gas, a systematic study of the ideas laid out above must commence. (Additional demonstrations of HG imaging have recently been reported at 15 mT [14]). The goal of our research here was to begin this exploration, first, by developing appropriate apparatus, and second, by performing in vitro and in vivo CPMG measurements [15] using hyperpolarized ^{3}He. The results are compared most extensively with those made at 0.1 T [8,9], as this is the lowest field at which the experimental parameters associated with HG lung imaging have previously been tested.

2. Apparatus

2.1. B_0 and B_1 coils

For this first set of measurements, we have employed a previously made B_0 magnet. The magnet consists of seven co-axial coils each of 144 turns of 2 mm diameter copper wire wound on an annular aluminum frame. The relative orientation of the coils is shown in cross-section in Fig. 1. The relative homogeneity of the B_0 field is only ~2000 ppm over a typical lung volume ($\Delta x \Delta y \Delta z = 15 \times 15 \times 30\,\mathrm{cm}^3$). The magnet was driven by a standard laboratory power supply and could maintain fields up to 6 mT (for 8.7 A, 940 W) without forced cooling. The bore of the magnet is along the vertical (Z-direction), and the entire construction is supported on an aluminum frame (not shown) with the bottom coil being
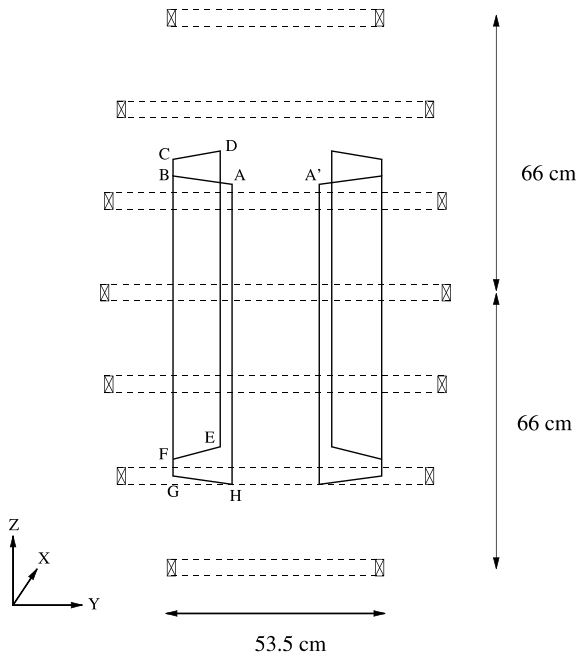
Fig. 1. Diagram of the B_0 and B_1 coils. The coils of the B_0 magnet are shown in cross-section: six coils (two each of mean diameter 78.0, 71.5, and 53.5 cm) are placed symmetrically (at 22.5, 44.5, and 66.0 cm, respectively) about the central coil, which has a mean diameter of 79.5 cm. For clarity, the B_1 coils are rendered in 3-D; the corners are labeled alphabetically. All pertinent dimensions are given in the text.

75 cm above the floor. This provides sufficient room for an average sized person to enter from below and rest standing during measurements.

The subject stands facing the X-direction, with chest centered within the two "C-shaped" coils (shown in Fig. 1) that generate the RF field, B_1, along the Y-direction. These coils were wound on a PMMA (poly(-methyl methacrylate)) frame with 11 outer turns (wound A through H) and 9 inner turns (wound B,C,F,G). The outer sections ($\overline{AB} = 15.4$ cm) make a 109° angle with the inner sections ($\overline{BC} = 32.0$ cm); the height of the coils is 72 cm and they are separated from one another by a distance $\overline{AA'} = 15.6$ cm. The coil was designed (using home-written software) as an inductor to produce an RF field homogeneous to within 5% over a typical lung volume. (This was confirmed by mapping with a small search coil.) To avoid spurious current paths, copper wire with a relatively thick insulating layer (1.4 mm diameter wire covered by a 0.7 mm layer of plastic) was used to keep adjacent windings well separated, thereby minimizing internal capacitance and maintaining a sufficiently high self-resonance of 350 kHz. The coil was tuned to the Larmor frequency with a series capacitor to obtain a convenient low impedance ($Z_1 \sim 50\,\Omega$, $Q_1 = 12$). It was driven by a homebuilt RF amplifier (with APEX PA46 operational amplifiers) and could produce a π-pulse at 100 kHz ($B_0 \sim 3$ mT) in a duration of $T_{RF} = 0.8$ ms. Gating and dephasing of the RF pulse were controlled via homebuilt circuitry. The reference

frequency came from the oscillator output of an EG&G 7265 lock-in amplifier, also used for NMR signal detection.

2.2. Detection coils

The detection system consists of four rectangular coils: two main coils (each of 10 turns and area 34×40 cm^2) at the front and back of the chest, and two smaller *compensation* coils (each of 40 turns but with 1/4 the area of the main coils) on either side of the chest. The main coils are separated by 26 cm, the compensation coils by 50 cm. The coils were arranged symmetrically about the center of the B_1 coil, and face the X-direction perpendicular to the B_1 field. The compensation coils were made smaller due to space limitations inside the B_0 magnet, but have the same flux (i.e. area × number of turns) as the main coils. They were added to the circuit, as sketched in Fig. 2, to increase the signal-to-noise ratio: the two sets of coils are connected in series, but with opposite polarity, which suppresses external noise signals while augmenting the internal NMR signal.

To measure the ^{3}He NMR signal, the coil system was tuned globally to the Larmor frequency ($Q = 32$), and the voltage signal was detected using the lock-in amplifier with differential input.

Typical noise levels at the lock-in output are shown in Fig. 3. The use of the compensation coils reduced the background noise by a factor of 7, which was sufficient
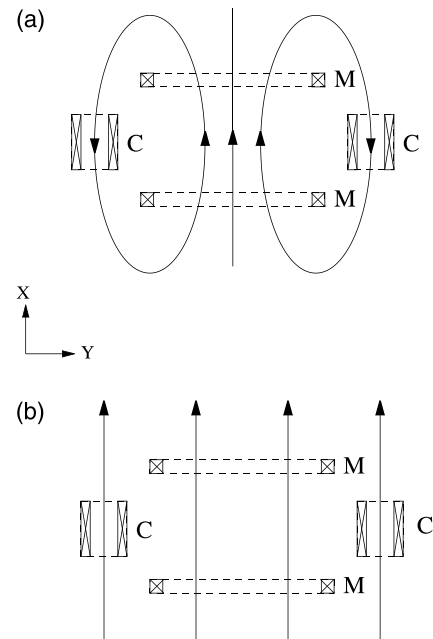

Fig. 2. Detection coil configuration. The compensation coils (C) are connected in series opposition with the main coils (M). Field lines are shown for: (a) an internal NMR signal, which is augmented by the compensation coils, (b) an external homogeneous noise signal, which is nullified by the compensation coils.
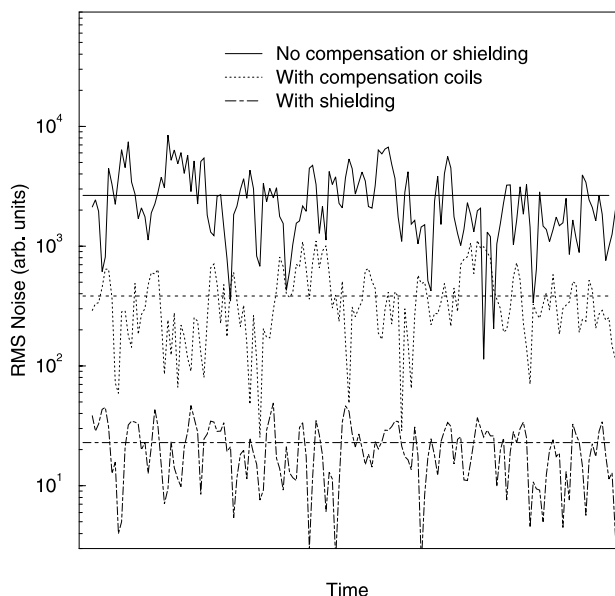
Fig. 3. Time sample of noise at lock-in output. Horizontal lines give the average value as calculated over 4 s (for clarity, only 80 ms of data are shown). With the use of the compensation coils (dotted line), the background noise (solid line) was reduced by a factor of 7. A further reduction, by a factor 17, was gained by enclosing the experiment with copper shielding (dot-dashed line).

to observe the desired NMR signal and make global measurements of the ADC. However, to obtain the necessary resolution for regional measurements, the entire experiment eventually had to be enclosed within a Faraday cage. This brought a further reduction in noise by a factor of 17 as shown in Fig. 3. The shielding (0.5 mm copper sheet) was effective in reducing external noise sources to levels below that of the intrinsic noise of the detection system (dominated by the Johnson noise of the coils). Under these conditions, the SNR was slightly better without the use of the compensation coils, as the added noise owing to their large impedance was not offset by their contribution to the signal.

2.3. Gradient coil for diffusion measurements

A gradient coil was made from two pairs of anti-Helmholtz coils (two 7-turn coils separated by 51.6 cm, and two 1-turn coils separated by 20.7 cm) wound on the B_1 coil frame. The combination of these coils produces a linear gradient $dB_0/dz = 95\,\mu T/m/A$. Measurements using a calibrated gradiometer [16] showed the gradient field to be homogeneous to within 5% over the typical lung volume. The gradient coil was driven by a Kepco 50-8M bipolar power supply with current switching times $< 25\,\mu s$. Eddy-currents generated in the aluminum frame of the B_0 magnet have been observed to hamper fast gradient switching by $\sim 15\%$, and to have a decay time of 800 μs. Pre-emphasis was used to compensate for their effect, and the desired gradient is obtained to $\pm 3\%$

of the change after 100 μs and to $\pm 0.5\%$ of the change after 300 μs.

2.4. Gas production

Production of the hyperpolarized ^{3}He was done in-house using the technique of metastability exchange optical pumping [17,18]. The gas was polarized at a pressure of about 3 mbar, within a homogeneous magnetic field of 0.9 mT, using a 2W ytterbium fiber laser (Keopsys YFL-1083-20). The pumping was done in a 50 cm long optical cell. The flow of gas through the cell was controlled via the combination of a flow regulator and a peristaltic compressor [19], which is used to extract the polarized gas from the optical cell and accumulate it in a storage cell. With flow rates around 2 cm^3 of gas at standard pressure per minute, a polarization of 30–40% could be achieved in the storage cell. Typically, 40 standard cm^3 of helium (1.8 mmol) were used for each measurement.

3. Method

When the gas was required for an experiment, it was pumped back via the peristaltic compressor into a 1 L plastic bag (a Tedlar gas sampling bag from Jensen Inert Products) to be carried to the measurement apparatus. High purity nitrogen was used as a neutral buffer gas to inflate the bag with a total amount of gas usually of order 0.5 L. The relaxation time T_1 of the gas in the bag is ~ 20 min, so experiments were designed to commence soon after this transfer had been made.

The extraction and transport of the gas was done in earth's field only, the optical pumping field and the NMR field having both been switched off. Just prior to measurement, and with the bag of gas inside the apparatus, the B_0 magnet current was ramped back up. In vitro measurements were performed in the bag. In vivo measurements were performed, with governmental approval, using 4 healthy adults who were fully informed about the procedures. While standing within the detection coils, the subject exhaled normally, inhaled the gas directly from the bag, and then further inhaled air to completely fill the lungs. The subject was then required to hold his breath during the acquisition time (typically 5 s or less).

All data presented in this paper were taken at 102 kHz (~ 3 mT) using CPMG echo sequences [15]. A $90°_x$ RF pulse ($T_{RF} = 0.4$ ms) was followed by a train of $180°_y$ RF pulses ($T_{RF} = 0.8$ ms) to refocus the transverse magnetization at a regular interval T_{CP}. Spatially non-selective tipping was obtained with a good angle accuracy by switching off any applied gradient at least 400 μs before the beginning of the RF pulses (see Appendix A). A PC running lab-written software was used to manage

the RF and gradient pulse sequencing, as well as to collect data directly from the lock-in amplifier via an A/D converter.

For a CPMG sequence, the transverse magnetization has a decay time $T_{2'}$ that can be written as

$$\frac{1}{T_{2'}} = \frac{1}{T_2} + \frac{1}{T_{2,\text{diff}}}. \tag{1}$$

The first term on the right-hand side is the inherent relaxation rate of the system, the second term represents additional relaxation resulting from diffusion in a non-uniform magnetic field, due to an applied field gradient and/or the magnet inhomogeneities. For a uniform applied gradient G, $T_{2,\text{diff}}$ can be expressed in the case of free gas diffusion as

$$T_{2,\text{diff}} = \frac{12}{D(\gamma k G T_{\text{CP}})^2}, \tag{2}$$

where D is the coefficient of diffusion and the factor k corrects for the time variation of the applied gradient, which is switched off during the RF pulses. For a rectangular gradient pulse, this correction factor is given as

$$k = \sqrt{\delta^2 (3T_{\text{CP}} - 2\delta)/T_{\text{CP}}^3}, \tag{3}$$

where $\delta \leq T_{\text{CP}}$ is the duration of the gradient [20].

CPMG measurements were made for different values of T_{CP} (3.6–90 ms) and applied gradient G (0–660 μT/m). For those measurements involving finite G, global or regional values of D were extracted using Eq. (2). This formula remains valid here, since over the length $\Delta z \sim \pm 15$ cm of the lung these relatively small applied gradients result in additional longitudinal (transverse) field components that are at least a factor 30 (60) smaller than the uniform 3 mT field [11].

For in vitro measurements in the bag, this should almost exactly correspond to D_{HeN2}, the coefficient for free diffusion of ^{3}He in N_2 (see Appendix B). For in vivo measurements, the extracted value of D was considered an apparent diffusion coefficient (ADC) for the restricted diffusion of ^{3}He in the gas mixture inside the lung.

4. Results

Preliminary measurements of the B_0 homogeneity were made via NMR on a sealed cell ($\sim$75 cm^3) of low pressure ^{3}He gas. The use of a small set of receive coils gave excellent SNR ($\sim$100) despite the low pressure of the gas (1–6 mbar). The gas in the cell was optically polarized in situ, which allowed the B_0 field to be mapped with relative ease. At each position an FID was recorded following a 90° RF pulse; the frequency of the signal gave the local field strength, whereas T_2^*, the decay time of the FID at $1/e$ of its initial value, gave a measure

of local gradients. Measurements were made at fields of 6 and 3 mT. In both cases, frequency measurements conformed to the theoretically calculated field map of the magnet. Furthermore, values of T_2^* were found to be twice as long at the lower applied field, which confirmed that local fields and their gradients were still dominated by the magnet at this level. To minimize residual gradients, we chose to operate at 3 mT.

To display the operation of the apparatus as well as some of the characteristics of ^{3}He gas NMR, a collection of CPMG spin echo data is shown in Fig. 4. These measurements were made with the Faraday cage and exhibit excellent SNR's of 200–300. The repetition rate was $T_{\text{CP}} = 24.8$ ms. The time axes of the graphs are broken to accentuate the evolution of the echoes. Data shown in the top panel were taken in vivo with zero applied gradient, and exhibit an echo amplitude that decays little over the timescale shown ($T_{2'} \sim 3.3$ s). The decoherence time $T_2^* \sim 10$ ms (Full Width Half Maximum), and the corresponding spread in the frequency domain, 90 Hz FWHM, are consistent with the inhomogeneity of the B_0 field over this volume. This suggests that tissue susceptibility gradients contribute little to the relaxation observed here. Data shown in the middle panel were taken in vivo with $G = 380$ μT/m. As a result of the strong applied gradient, the echoes are much
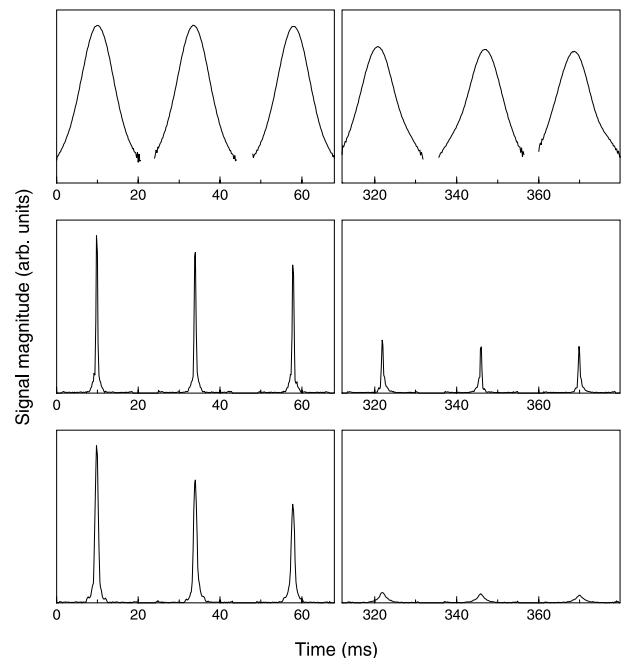

Fig. 4. CPMG spin echo data with $T_{\text{CP}} = 24.8$ ms. Saturation of the detection system occurs between echos due to the strong RF pulse, and the corresponding data are not displayed. Top panels: in vivo, zero applied gradient. Echo amplitude shows little decay after 300 ms; residual magnet gradients give a $T_2^* \simeq 10$ ms. Middle panels: in vivo, $G = 380$ μT/m. The strong applied gradient shortens $T_{2'}$ and T_2^*. Bottom panels: in vitro, $G = 240$ μT/m. With free diffusion, a shorter $T_{2'}$ is obtained despite the lower applied gradient.

more narrow (shorter T_2^*) and show a marked decay in amplitude (shorter $T_{2'}$, now 0.34 s). Data shown in the bottom panel were taken in vitro with $G = 240\,\mu\text{T/m}$; to obtain a decay rate similar to that which was observed in vivo, the value of the applied gradient has to be lowered to compensate for a faster rate of diffusion (see Eq. (2)). This result highlights the difference between the restricted diffusion of ^3He inside the lung and the free diffusion it experiences in the bag.

Apart from the slowest decays recorded in vivo (see Section 4.1), no significant deviation from monoexponential behavior was observed in the diffusion weighted echo decays . To extract values of $T_{2'}$ from our data, monoexponential fits were made to the square of the echo amplitudes, or the square of their Fourier components. The use of power data, rather than the magnitudes, yields a more reliable result as the latter contains a non-zero baseline that leads to an overestimation (underestimation) of decay times if it is left in (subtracted out) [21]. For extremely long decay times, such as those shown in Fig. 5, we found that the results from various fitting procedures did not vary significantly (this is further discussed in Section 4.3).

4.1. Fast repetition CPMG with no applied gradient

Measurements made in zero applied gradient using a very short $T_{CP} = 3.6$ ms are shown in Fig. 5. For such a fast repetition rate the lock-in amplifier had to be operated with lower gain which caused a slight decrease in the SNR. The excellent homogeneity of the B_1 field
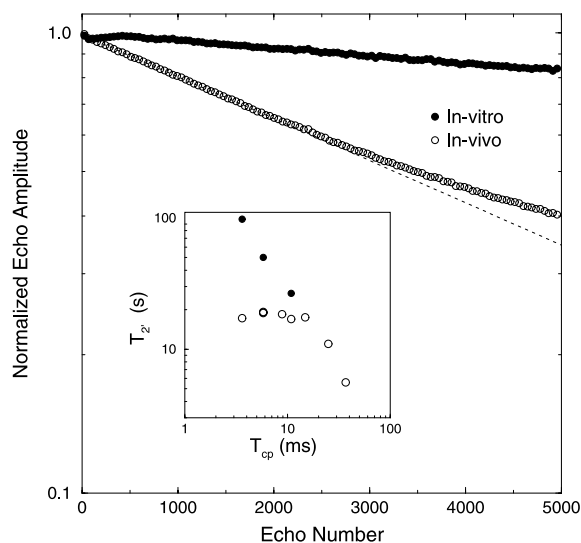

Fig. 5. Fast repetition CPMG sequence ($T_{CP} = 3.6$ ms) in zero applied gradient. (For clarity, each symbol represents the average of 40 consecutive points.) The transverse relaxation rate is much slower in vitro (●) than in vivo (○). The dotted line indicates the initial, in vivo, decay rate; this rate slows in time as the O_2 concentration decreases. Inset: $T_{2'}$ for various T_{CP} in zero applied gradient. At small T_{CP}, the in vivo $T_{2'}$ is limited by T_1 relaxation due to O_2.

allowed for the refocusing of thousands of echoes with very little loss per RF pulse (see Appendix A). The extremely low power radiated at this frequency allowed these measurements to be safely performed in vivo as well.

It is clear from Fig. 5, that there is marked difference in decay rate between the in vitro ($T_{2'} \sim 98$ s) and in vivo ($T_{2'} \sim 17$ s) results. For ^3He in the bag, the transverse relaxation at $T_{CP} = 3.6$ ms would have been limited by the following: diffusion of the gas in the residual magnet inhomogeneities, π-pulse losses, or a combination of both; the longitudinal relaxation, $T_1 \sim 20$ min, was too long to have made a contribution. As shown in the inset of Fig. 5, the $T_{2'}$ in the bag dropped rapidly with increased T_{CP} indicating that diffusion was the dominant relaxation mechanism above $T_{CP} = 3.6$ ms. By contrast, the in vivo $T_{2'}$ hovered around a much lower value (17–19 s for this subject, 16–22 s for the other three subjects) before falling off at T_{CP} around 15 ms. The $T_{2'}$ values in this *plateau* region are comparable to the oxygen-limited T_1 values ($\sim$12–20 s) measured for ^3He in the lung by MRI at high field [22,23]. Complementary global measurements of T_1 (decays monitored using small angle tipping pulses, as described in [8]) and $T_{2'}$ (with no applied gradient) have been performed in vitro at 2 mT in a different NMR apparatus. Decay times of several minutes have been obtained for small amounts of ^3He mixed with pure N_2, while $T_{2'} = T_1 = 13$ s were measured for ^3He in air at room pressure and temperature. This strongly suggests that the constant $T_{2'}$ we observed at short T_{CP} was indeed due to the nominal O_2 concentration in the lung. To corroborate this finding, similar measurements were made where the subject did not inhale air following a 1-L bolus of HP gas. In this case, $T_{2'}$ values greater than 30 s and as high as 36 s were observed (for $T_{CP} = 5.8$ ms), consistent with a longer T_1 due to a lower oxygen concentration.

Another strong signature of O_2-induced relaxation can be seen in the main graph of Fig. 5. The decay rate in vivo was not constant, as was seen in vitro, but instead slowed down over time as the O_2 concentration in the lung decreased. This is highlighted by the dashed line which indicates the initial decay rate of 17 s. A full fit to the data (not shown) reveals that the echo decay rate, and hence the O_2 partial pressure, decreases linearly with time. This has also been observed by the direct measurement of the ^3He T_1 in the lung [24].

4.2. Global diffusion measurements

A compilation of all our diffusion measurements (taken with and without the Faraday cage, and using two of the subjects only) is shown in Fig. 6. These measurements were made with a minimum T_{CP} of 8.8 ms. The general behavior seen here is compared with the recently published results of reference [9] taken at
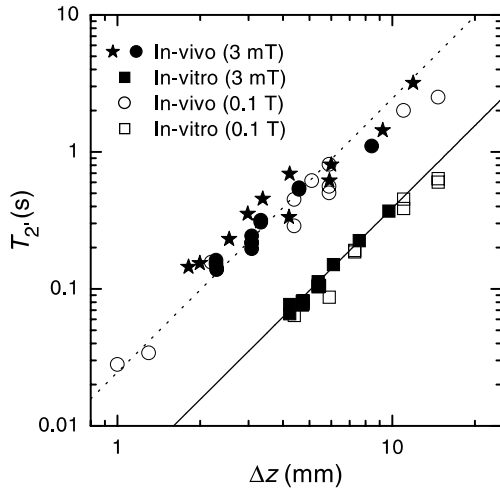
Fig. 6. Summary of CPMG results plotted as $T_{2'}$ versus an effective pixel size Δz (see text). Data are shown for in vivo (circles, stars) and in vitro (squares) measurements; our results at 3 mT (closed symbols) are compared to those of [9] taken at 0.1 T (open symbols). The stars are the initial 3 mT measurements performed without the Faraday cage. The solid line is the theoretical response using D_{HeN2}. The dashed line was generated using $D_{HeN2}/6.3$; it acts to guide the eye and to highlight the restricted diffusion observed in the lung.

Table 1
Table of global ADC values computed from in vivo CPMG measurements

	ADC (mm^2/s)	Error (mm^2/s)
All 3 mT data	14.2	±0.6
0.1 T data	22	±1.5
All 3 mT data	11.9	±3.4
Initial 3 mT data	11.3	±4.2
3 mT data in cage	12.4	±2.5
0.1 T data	16	±5

Upper two lines: values from global linear fits (±SE) of the data (squares of pixel sizes versus $T_{2'}$). Lower four lines: values deduced in each measurement using Eq. (2) (individual ADC values ±SD).

0.1 T with a different set of two subjects. The data is plotted as $T_{2'}$ versus $\Delta z = 2\pi/(\gamma k G T_{CP})$, which appears in Eq. (2) as the natural length scale for relaxation due to diffusion. Δz actually differs from the usual pixel size $2\pi/(\gamma G \delta)$, which sets the resolution of any MR image and provides a useful forum to discuss the results, but the two lengths have similar values in our experiments since $\delta \approx T_{CP}$.

It is clear from Fig. 6 that results at 3 mT (closed symbols) and 0.1 T (open symbols) exhibit the same trend: for a given value of Δz, there is a longer $T_{2'}$ in vivo owing to the restricted diffusion of the ^{3}He in the small airspaces of the lung. This is fortunate from the point of view of lung imaging, as more time can be had to obtain the desired image resolution. To extract diffusion coefficients, noting that $1/T_2$ is negligible for these data, linear fits (through the origin) were made to the data of Fig. 6 plotted as Δz^2 versus $T_{2'}$. This procedure gives more weight to measurements with longer $T_{2'}$, which have a higher SNR, and is thus preferred to a linear fit of Δz^{-2} versus $1/T_{2'}$. For in vitro results, we obtained a value of $79.5 \pm 1 \, mm^2/s$, in perfect agreement with the expected free diffusion coefficient (see Appendix B). This is likely to be fortuitous since the gradient calibration is not accurate to better than 1% and the ambient pressure and temperature were not precisely measured during the experiments. The solid line in Fig. 6 was drawn using this value to show the theoretical response for the free diffusion of ^{3}He in N_2.

Using all our in vivo measurements we obtained a value for the global ADC in the lung of $14.2 \pm 0.6 \, mm^2/s$,

whereas results from reference [9] give $22 \pm 1.5 \, mm^2/s$ (see Table 1).

On average our measurements give a global ADC that is on the order of $D_{HeN2}/6.3$ (the dashed line in Fig. 6). In contrast with in vitro measurements, a possible deviation from quadratic dependence and a large scatter are observed in Fig. 6 for in vivo measurements. The small quoted statistical error on the ADC values in the lung are thus misleading, and it is much more relevant to extract one ADC value from each measurement and to relate the scatter to differences between measurements. The corresponding results are given in the lower part of Table 1. The possible deviation from quadratic dependence in Fig. 6 could not arise from the anisotropy of the lung structure at microscopic length scales, as probed using strong bipolar gradients for diffusion weighting [25]. In this experiment, it would rather indicate the complex variation of the gas confinement over the explored length scales (2–10 mm). Over the range of diffusion times examined here, the scatter in the data is likely dominated by differences that exist in the physiology of the subjects, and in the degree of lung inflation. In light of these last two points, it is interesting to note that the smallest scatter was obtained for a set of measurements that happened to be taken in a single subject only and where similar breathing maneuvers were used (data in the Faraday cage, solid circles in Fig. 6).

It is also worthwhile noting that average ADC values reported here and in [9] tend to be lower than those of other healthy subjects that have recently been measured at 1.5 T using bipolar gradient pulses (17–25 mm^2/s from [26] or 16–30 mm^2/s from [27]). Certainly, physiology and imaging parameters could account for the observed discrepancies, however, one should also consider the difference in probed length scales as argued in [9].

4.3. Regional diffusion measurements

Each recorded echo contains information on the distribution of the polarized gas along the applied gradient axis (here, the vertical Z-axis oriented from feet
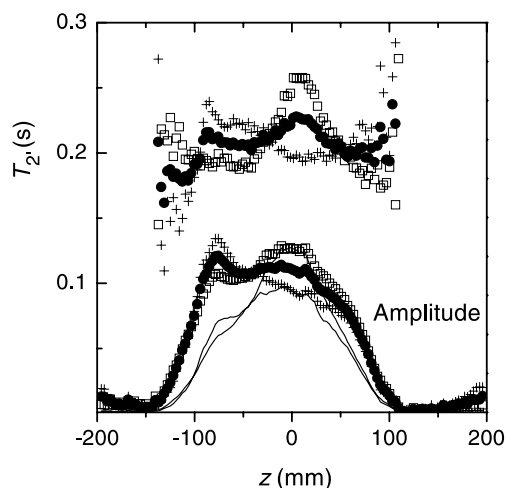
Fig. 7. 1D images of the inital amplitudes (lower traces, arbitrary scale) and local $T_{2'}$s (upper traces) from in vivo measurements in the Faraday cage with opposed applied gradients ($|G| = 660\,\mu\text{T/m}$) and otherwise identical conditions ($T_{CP} = 15.8\,\text{ms}$, $\delta = 13\,\text{ms}$, sampling frequency 10 kHz). Solid lines: uncorrected amplitudes with limited bandwidth effects. Open squares, crosses: corrected amplitudes and fitted $T_{2'}$s for the measurements. Filled circles: average values of the results, which eliminate the main effect of B_0 inhomogeneities (see text).

to head for a standing subject). FFTs of the spin echoes thus provide a series of 1D images with a nominal resolution given by the pixel size defined in the previous section. Provided that the SNR is large enough, a pixel by pixel analysis of the decays can be performed to obtain Z-profiles of the initial gas distribution and of the local decay time. Examples of results of such analyses are shown in Fig. 7 for two in vivo measurements performed with opposite gradient directions. For each measurement, the fitted initial amplitudes (solid lines) and decay times are obtained from non-linear least squares (NLLS) exponential fits of the power spectra (i.e., fitting, for each pixel, the squares of the amplitudes of the echoes by a single exponential decaying to the noise level). The fitted amplitude profiles are used to compute the actual gas distribution profiles (symbols) by simply correcting for the acquisition system bandwidth (in Fig. 7, the 395 mm field of view (FOV) corresponds to a frequency range of 10 kHz, while the FWHM bandwidth of the detection coil is 5.6 kHz). The SNR in the central region of the lung with highest signal intensity is 180 (signal amplitude in Fig. 7 divided by standard deviation between echoes in similar recordings without polarized gas). The noise level increases near the edges of the FOV due to the growing influence of the amplifier noise in the bandwidth-corrected data.

A difference in profiles obtained for opposite directions of the applied gradient was systematically observed in all experiments, both in vivo and in vitro. It is attributed to the rather strong magnet inhomogeneities at the position of the measurements, which result in a non-uniform value of the total gradient. It is much weaker on

the field axis, it scales with B_0 (as was checked at 1.5 mT) and it is relatively larger at reduced applied G. Fig. 7 clearly shows that an apparent excess (lack) of signal amplitude is correlated to a longer (shorter) $T_{2'}$ than the average: both effects result from a locally decreased (increased) value of the total field gradient. To first order, the averages of the values obtained from experiments performed with $\pm G$ (the filled symbols in Fig. 7) should thus reproduce the true gas distribution profile and the true $T_{2'}$ profile which would be directly measured in a homogeneous B_0 field.

A clear non-uniform distribution of the average signal is observed in the high intensity region, however, it may result from the imperfectly compensated effects of the $\pm G$ measurements. The average $T_{2'}$ profile is quite uniform over most of lung ($\pm 5\%$ over the high signal intensity region), and the observed variations cannot be safely ascribed to actual ADC differences in spite of the high SNR. Regional dependence of the measured ADC in the normal human lung has been observed at 1.5 T [28], with 20% lower ADC values in the posterior part of the lungs of a supine lying subject (this is attributed to the known gravity-induced differences, e.g., of alveolar inflation, in the normal lung). As is discussed in reference [9], the length scale involved in such measurements (typically 0.3 mm) is much smaller than the length scale Δz in a CPMG measurement, and this may impact on the ADC values.

For all measurements performed in the Faraday cage, the high SNR allows to perform a local ADC analysis and to apply the corrections required to obtain local or global values of the ADC. However, the reduced SNR of all initial measurements (without the Faraday cage) prevented us from making such corrections, and the global $T_{2'}$ values in Fig. 6 have been computed by NLLS exponential fits of the total areas of the power spectra of the echoes. We have checked on all high SNR data (both for $+G$ and $-G$) that this procedure actually introduces little bias (<10%) on the global $T_{2'}$ compared to the true average, much less in fact than the rather large scatter of the in vivo results.

5. Prospects

In this paper we have presented NMR measurements of ^{3}He in the human lung made with a simple, homebuilt system operating at 3 mT. With this device we were able to demonstrate for the first time some of the proposed benefits of performing HG imaging at very low field, most notably, human scale MR with good SNR using a very simple scanner design. Using a simple wire-wound coil, we were able to generate a B_1 field of sufficient homogeneity to observe very long CPMG decay rates without being obscured by π-pulse losses or affected by tissue susceptibility effects. Thanks to the full use of the

available magnetization in a CPMG experiment, this provides an accurate way to measure the O_2 concentration and its time evolution with small quantities of polarized gas. The assessment of the potential interest of these measurements, and their extension to regional measurements must now be performed.

Good SNR was obtained in the 1D profiles even using modest quantities of gas and unsophisticated NMR coils. With additional gradient coils, 2D and 3D imaging is expected to provide results similar to those already obtained in a commercial 0.1 T apparatus [9], with the added flexibility allowed by the ultrafast RF repetition and the very long intrinsic T_2. This potential to perform quality lung imaging and accurate ADC mapping at very low field in a *standing* subject will be fully used when a dedicated B_0 field of adequate homogeneity over the lung volume—a system rather easy to design and build—will be operational.

Acknowledgments

Appendix A. Field inhomogeneities and tipping angle accuracy

In the rotating frame synchronous with the near-resonant component of the RF $\mathbf{B}_1$ field, the magnetization tipping at a given point $\mathbf{r}$ results from the precession during a time T_{RF} around the effective field $\mathbf{B}_{eff} = \mathbf{B}_0(v_{RF} - v_0(\mathbf{r}))/v_{RF} + \mathbf{B}_1(\mathbf{r})$, where $v_0(\mathbf{r})$ is the local Larmor frequency and v_{RF} the frequency of the $\mathbf{B}_1$ field. Noting Ψ the angle of $\mathbf{B}_{eff}$ with the Z direction (that of the average $\mathbf{B}_0$ field, see Section 2.1), the actual tip angle θ at position $\mathbf{r}$ is given by

$$\cos \theta(\mathbf{r}) = \cos^2 \Psi + \sin^2 \Psi \cos (\gamma B_{eff} T_{RF}). \quad (A.1)$$

180° pulses cannot be exactly obtained except at resonance ($\Psi = \pi/2$), and the largest tip angle which can be obtained is 2Ψ for the optimal pulse duration $T_{RF}^{opt} = \pi/\gamma B_{eff}$. We now consider situations where imperfect 180° pulses result from small deviations from the resonance conditions and small spatial variations of B_1. Setting the pulse duration to its optimal value for the average B_1 field (assuming resonance conditions), the tip angle computed from Eq. (A.1) depends on position through the local values of B_0 and B_1 as shown in Fig. A.1.
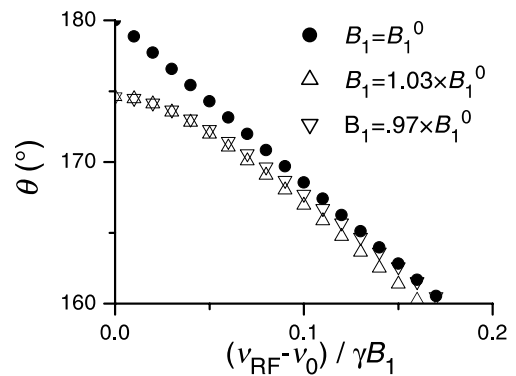

Fig. A.1. Computed actual tip angle obtained for imperfect 180° pulses, due to an off-resonance RF frequency (horizontal axis) and imperfect RF amplitude (open symbols).

In our experiment, the RF field is uniform to ±3%, and $\gamma B_1 = 625$ Hz. The B_0 field is ramped up just before data acquisition, and the resonance condition at the center of the apparatus is obtained with a reproducibility and a stability of ±50 Hz. In the absence of applied gradients, the field inhomogeneity over a typical lung volume is estimated from FFTs of spin echoes such as in Fig. 4 (top panel). The 90 Hz FWHM spread (200 Hz spread for 90% of the spectrum area) corresponds to $v_{RF} - v_0(\mathbf{r}) = \pm 45$ Hz (± 100 Hz). Finally, when switched gradients are used, their residual value during the RF pulses is lower than 0.5% of the applied value (at most ±5 kHz over a 395 mm FOV), i.e., ±15 Hz over a lung volume. From the plots in Fig. A.1, actual angles of 170° (160°) are expected for detunings of 50 Hz (100 Hz). Since angle errors α are expected to induce a loss $\alpha^4/32$ for each pulse in a CPMG sequence [29], the corresponding values for this loss are 2.9×10^{-5} (4.6×10^{-4}). This is consistent with the negligible contribution from pulse losses inferred in all our experiments, even when thousands of echoes are recorded as in Fig. 5.

Appendix B. Value of D in several gas mixtures

The free diffusion coefficient D in Eq. (2) depends on the gas temperature T, pressure P, and composition. For helium, there is an additional effect of the isotopic nature. Data have been published for diffusion in helium based on calculations of transport coefficients for accurate potentials [30] and on NMR measurements in ^{3}He [31,32]. Data for binary diffusion of the ^{4}He–N_2 [33,34] and ^{4}He–O_2 [34] systems have been obtained by mass-diffusion measurements. Using a classical theory for transport in dilute gases [35], we provide numerical formulas to compute D for a ^{3}He gas with partial pressure P_3 in a gas containing other components (^{4}He, N_2, O_2) with partial pressure P_4, P_{N2}, and P_{O2}, in the

simple case of uniform temperature and partial pressures.

We first evaluate the self- and binary-diffusion coefficients of ^{3}He, D_3, D_{34}, D_{3N2}, and D_{3O2}. With notations of reference [35],

$$D_3 = \frac{3}{16} \frac{\sqrt{2\pi(k_B T)^3/m_3}}{P_3 \pi \sigma^2 \Omega^{(1,1)*}} \qquad (B.1)$$

where k_B is the Boltzmann constant, m_3 the ^{3}He atomic mass, $\pi\sigma^2$ the collision cross-section in a rigid-sphere model and $\Omega^{(1,1)*}$ a T-dependent factor depending on the actual interatomic potential. The pressure-independent reduced diffusion coefficient $\mathcal{D}_3 = P_3 D_3$ has an apparent $T^{3/2}$ temperature dependence (actually assumed in [32]), but this is not exact for a real gas. For helium (^{3}He, ^{4}He and isotope mixtures), the computed values in the 200–600 K range [30] can be accurately reproduced (within 0.2%) by a power law $\mathcal{D}_i(T) \propto T^{1.71}$. For a binary mixture in which ^{3}He (with negligible partial pressure) diffuses in another component i, D_{3i} is given by Eq. (B.1) in which the ^{3}He mass is replaced by the reduced mass $\mu_{3i} = m_3 m_i/(m_3 + m_i)$, P_3 by P_i (the foreign gas pressure) and $\Omega^{(1,1)*}$ depends on the involved interaction potential. The reduced diffusion coefficient $\mathcal{D}_{3i} = P_i D_{3i}$ again only depends on temperature. For N_2, the values measured in the 300–800 K range [33] can be nicely fit by $\mathcal{D}_{4N2}(T) \propto T^{1.65}$. For both N_2 and O_2, the ratios of the measurements of [34] provide the same exponent 1.68 but this determination is less accurate due to the small temperature interval (300 and 323 K). We thus choose to use the same exponent 1.65 for N_2 and O_2. All these experimental data have been obtained for ^{4}He, and the faster diffusion of ^{3}He can be evaluated using the ratio of the relevant reduced masses. This procedure provides the correct values within 0.1% compared to the diffusion of helium [30] or helium–hydrogen [36] isotope mixtures. This results from the negligible effect of quantum statistics on the binary collisions at room temperature, and is even more accurate for collisions with a heavier molecule. These isotope effects and the numerical formulas for $\mathcal{D}_3(T)$ and $\mathcal{D}_{3i}(T)$ are collected in Table B.1.

Table B.1
First 4 lines: isotope effect on the self- or binary-diffusion coefficients of helium at given temperature and pressure

$D_3/D_4 = \sqrt{4/3}$
$D_{34}/D_4 = \sqrt{7/6}$
$D_{3N2}/D_{4N2} = \sqrt{31/24}$
$D_{3O2}/D_{4O2} = \sqrt{35/27}$
$\mathcal{D}_3 = P_3 D_3 = 1.997 \times (T/300)^{1.71}$
$\mathcal{D}_{34} = P_4 D_{34} = 1.868 \times (T/300)^{1.71}$
$\mathcal{D}_{3N2} = P_{N2} D_{3N2} = 0.811 \times (T/300)^{1.65}$
$\mathcal{D}_{3O2} = P_{O2} D_{3O2} = 0.857 \times (T/300)^{1.65}$

Last 4 lines: numerical expressions to compute the reduced diffusion coefficients $\mathcal{D}(T)$, in units of atm $\times$ cm^2/s (1 atm = 1.013 $\times$ 10^5 Pa), with the temperature T in Kelvin.

The free diffusion coefficient D in a gas mixture is finally given from these reduced diffusion coefficients by

$$\frac{1}{D} = \frac{P_3}{\mathcal{D}_3(T)} + \frac{P_4}{\mathcal{D}_{34}(T)} + \frac{P_{N2}}{\mathcal{D}_{3N2}(T)} + \frac{P_{O2}}{\mathcal{D}_{3O2}(T)}. \qquad (B.2)$$

Eq. (B.2) can be applied for instance to the gas mixtures used for the in vitro measurements of Fig. 6, for which typically 30 cm^3 of ^{3}He were mixed to 1 L of N_2: for 1 atm at 20 °C, one obtains $D = 79.5\,\text{mm}^2/\text{s}$, slightly larger than $D_{3N2} = 78.1\,\text{mm}^2/\text{s}$. Eq. (B.2) can also be applied to evaluate the *free* diffusion coefficient for typical in vivo experiments, in which the inhaled dose (30 cm^3 of ^{3}He mixed with 0.5 L of N_2) mixes with the subject's lung contents ($\sim$5 L of O_2-depleted air, since the typical partial pressure of O_2 is 0.13 atm in vivo instead of 0.21 atm in room air). For 1 atm of this mixture at 37 °C, one obtains $D = 86.6\,\text{mm}^2/\text{s}$. This higher value is mostly due to the higher temperature, and to a lesser extent to the faster diffusion of helium in O_2.

References

[1] C.H. Tseng, G.P. Wong, V.R. Pomeroy, R.W. Mair, D.P. Hinton, D. Hoffman, R.E. Stoner, F.W. Hersman, D.G. Cory, R.L. Walsworth, Low-Field MRI of laser polarized noble gas, Phys. Rev. Lett. 81 (1998) 3785–3788.

[2] G.P. Wong, C.H. Tseng, V.R. Pomeroy, R.W. Mair, D.P. Hinton, D. Hoffman, R.E. Stoner, F.W. Hersman, D.G. Cory, R.L. Walsworth, A system for low field imaging of laser-polarized noble gas, J. Magn. Reson. 141 (1999) 217–227.

[3] M.S. Albert, G.D. Cates, B. Driehuys, W. Happer, B. Saam, C.S. Springer, A. Wishnia, Biological magnetic resonance imaging using laser-polarized ^{129}Xe, Nature 370 (1994) 199–201.

[4] M. Ebert, T. Grossmann, W. Heil, E.W. Otten, R. Surkau, M. Leduc, P. Bachert, M.V. Knopp, L.R. Schad, M. Thelen, Nuclear magnetic resonance imaging with hypolarized ^{3}He, Lancet 347 (1996) 1297–1299.

[5] P. Bachert, L.R. Schad, M. Bock, M.V. Knopp, M. Ebert, T. Grossmann, W. Heil, D. Hoffman, R. Surkau, E.W. Otten, Nuclear magnetic resonance imaging of airways in humans with use of hypolarized ^{3}He, Magn. Reson. Med. 36 (1996) 192–196.

[6] J.R. MacFall, H.C. Charles, R.D. Black, H. Middleton, J.C. Swartz, B. Saam, B. Driehuys, C. Erickson, W. Happer, G.D. Cates, G.A. Johnson, C.E. Ravin, Human lung air spaces: potential for MR imaging with hyperpolarized He-3, Radiology 200 (1996) 553–558.

[7] D.I. Hoult, P.C. Lauterbur, The sensitivity of the zeumatographic experiment involving human samples, J. Magn. Reson. 34 (1979) 425–433.

[8] L. Darrasse, G. Guillot, P.-J. Nacher, G. Tastevin, Low-field ^{3}He nuclear magnetic resonance in human lungs, C. R. Acad. Sci. Paris 324 (1997) 691–699.

[9] E. Durand, G. Guillot, L. Darrasse, G. Tastevin, P.-J. Nacher, A. Vignaud, D. Vattolo, J. Bittoun, CPMG measurements and ultrafast imaging in human lungs with hyperpolarized helium-3 at low field (0.1 T), Magn. Reson. Med. 47 (2002) 75–81.

[10] J.R. Mayo, M.E. Hayden, Hyperpolarized helium 3 diffusion imaging of the lung, Radiology 222 (2002) 8–11.

[11] A. Mohorič, J. Stepišnik, M. Kos, G. Planinšič, Self-Diffusion imaging by spin echo in earth's magnetic field, J. Magn. Reson. 136 (1999) 22–26.

[12] D. Norris, Phase Errors in NMR Images, in Second Annual Meeting of the Society of Magnetic Resonance in Medicine, 1037 (1985).

[13] E. Durand, PhD thesis (Paris,2001) pp. 173–178. Available from: http://tel.ccsd.cnrs.fr/documents/archives0/00/00/09/30/index.html (in french).

[14] A.K. Venkatesh, L.V. Kubatina, A.X. Zhang, C.-H. Oh, D. Balamore, F.A. Jolesz, M.S. Albert, In vivo MRI at 0.015 T using hyperpolarized xenon, Proc. Eighth Annual Meeting of the International Society of Magnetic Resonance in Medicine, Denver, CO, 2000, p. 2189.

[15] S. Meiboom, D. Gill, Modified Spin-echo method for measuring nuclear relaxation times, Rev. Sci. Instrum. 29 (1958) 688–691.

[16] V. Senaj, G. Guillot, L. Darrasse, Inductive measurement of magnetic field gradients for magnetic resonance imaging, Rev. Sci. Instrum. 69 (1998) 2400–2405.

[17] T. Chupp, S. Swanson, Medical imaging with laser polarized noble gases, Adv. At. Mol. Opt. Phys. 45 (2001) 51.

[18] G. Tastevin, Optically polarized helium-3 for NMR imaging in medicine, Phys. Scripta T86 (2000) 46–50.

[19] P.-J. Nacher, G. Tastevin, X. Maitre, X. Dollat, B. Lemaire, J. Olejnik, A peristaltic compressor for hyperpolarized helium, Eur. Radiol. 9 (1999) B18.

[20] E. Stejskal, J. Tanner, Spin diffusion measurements: spin echoes in the presence of a time-dependent field gradient, J. Chem. Phys. 42 (1965) 288–292.

[21] L. van der Weerd, F.J. Vergeldt, P.A. de Jager, H. Van As, Evaluation of algorithms for analysis of NMR relaxation decay curves, Magn. Reson. Imaging 18 (2000) 1151–1157.

[22] A.J. Deninger, B. Eberle, M. Ebert, T. Grossman, G. Hanisch, W. Heil, H.-U. Kauczor, K. Markstaller, E. Otten, W. Schreiber, R. Surkau, N. Weiler, ^{3}He-MRI-based measurements of intrapulmonary pO$_2$ and its time course during apnea in healthy volunteers: first results, reproducibility, and technical limitations, NMR Biomed. 13 (2000) 194–201.

[23] H.-U. Kauczor, X.J. Chen, E.J.R. van Beek, W.G. Schreiber, Pulmonary ventilation imaged by magnetic resonance: at the doorstep of clinical application, Eur. Respir. J. 17 (2001) 1–16.

[24] A.J. Deninger, B. Eberle, J. Bermuth, B. Escat, K. Markstaller, J. Schmiedeskamp, W.G. Schreiber, R. Surkau, E. Otten, H.-U. Kauczor, Assessment of a single-acquisition imaging sequence

for oxygen-sensitive ^{3}He-MRI, Magn. Reson. Med. 47 (2002) 105–114.

[25] D.M. Yablonskiy, A.L. Sukstanskii, J.C. Leawoods, D.S. Gierada, G.L. Bretthorst, S.S. Lefrak, J.D. Cooper, M.S. Conradi, Quantitative in vivo assessment of lung microstructure at the aveolar level with hyperpolarized ^{3}He diffusion MRIs, Proc. Natl. Acad. Sci. USA 99 (2002) 3111–3116.

[26] B.T. Saam, D.M. Yablonskiy, V.D. Kodibagkar, J.C. Leawoods, D.S. Gierada, J.D. Cooper, S.S. Lefrak, M.S. Conradi, MR imaging of diffusion of ^{3}He gas in healthy and diseased lungs, Magn. Reson. Med. 44 (2000) 174–179.

[27] M. Salerno, E.E. deLange, T.A. Altes, J.D. Truwit, J.R. Brookeman, J.P. Mugler III, Emphysema: hyperpolarized helium 3 diffusion MR imaging of the lungs compared with spirometric indexes—initial experience, Radiology 222 (2002) 252–260.

[28] M. Salerno, J.R. Brookeman, E.E. de Lange, J. Knight-Scott, J.P. Mugler III, Demonstration of an alveolar-size gradient in the healthy human lung: a study of the reproducibility of hyperpolarized ^{3}He diffusion MRI, in: Proceedings of Eighth Annual Meeting of the International Society of Magnetic Resonance in Medicine, Denver, CO, 2000, p. 2195.

[29] B. Cowan, Nuclear Magnetic Resonance and Relaxation, Cambridge University Press, Cambridge, 1997, Sect. 4.6.3.

[30] M.J. Slaman, R.A. Aziz, Accurate transport-properties and 2nd virial-coefficients for helium based on a state-of-the-art interatomic potential, Int. J. Thermophys. 12 (1991) 837–854.

[31] R. Barbé, M. Leduc, F. Laloë, Magnetic-resonance in an inhomogeneous radiofrequency field. II. Experimental verifications—measurement of the ^{3}He self-diffusion coefficient, J. Phys. Paris 35 (1974) 935–951.

[32] M. Bock, Simultaneous T2* and diffusion measurements with ^{3}He, Magn. Reson. Med. 38 (1997) 890–895.

[33] J. Liner, S. Weissman, Determination of the temperature dependence of gaseous diffusion coefficients using gas chromatographic apparatus, J. Chem. Phys. 56 (1972) 2288–2290.

[34] P.S. Arora, P.J. Dunlop, The pressure dependence of the binary diffusion coefficients of the systems He–Ar, He–N$_2$, He–O$_2$, and He–CO at 300 and 323 K: tests of Thorne's equation, J. Chem. Phys. 71 (1979) 2430–2432.

[35] J.O. Hirschfelder, C.F. Curtiss R.B. Bird, Molecular theory of gases and liquids, Second printing, Wiley, New York, 1964, p 527 (Chapter 8).

[36] W.L. Taylor, J.J. Hurly, B.A. Meyer, P.J. Dunlop, Binary diffusion coefficients of helium/hydrogen isotope mixtures, J. Chem. Phys. 103 (1995) 6959–6965.